Small-angle neutron scattering analysis in Sn-Ag Lead-free solder alloys: A focus on the Ag3Sn intermetallic phase

Shanthi Bhavan, J., Kadavath, G., Honecker, D. & Pazhani, A

DOI 10.1016/j.matchar.2024.114385
ISSN 1044-5803
ESSN 1873-4189

Publisher: Elsevier

Materials Characterization 217 (2024) 114385

Contents lists available at ScienceDirect

Materials Characterization

journal homepage: www.elsevier.com/locate/matchar

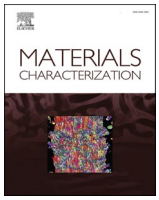

Small-angle neutron scattering analysis in Sn-Ag Lead-free solder alloys: A focus on the Ag_3Sn intermetallic phase

Jayesh Shanthi Bhavan [a,*], Gokulnath Kadavath [a], Dirk Honecker [b], Ashwath Pazhani [a]

[a] School of Mechanical Engineering, Coventry University, Coventry CV1 5FB, UK
[b] ISIS Neutron and Muon Source, Science and Technology Facilities Council, Rutherford Appleton Laboratory, Didcot OX11 0QX, United Kingdom

ARTICLE INFO

Keywords:
Lead-free
SANS
Neutron scattering
Phase analysis
Ag_3Sn scattering

ABSTRACT

This study addresses the critical need for lead-free solder alternatives in electronic manufacturing by investigating the microstructural characteristics of Sn-Ag solder alloys, focusing on the Ag_3Sn intermetallic phase. Utilizing Small-Angle Neutron Scattering (SANS), the study explored the phase interface and grain structure within Sn-Ag alloy to identify attributes that influence mechanical stability and performance. The research was structured around a comprehensive SANS analysis, complemented by Electron Backscatter Diffraction (EBSD) to expose the morphology and orientation of crystalline phases within the material. The investigation revealed distinct scattering patterns indicative of a multi-phase structure with a homogeneous distribution of fine Ag_3Sn precipitates within a β-Sn matrix. EBSD data confirmed these findings, showing a wide range of grain sizes and a random orientation distribution that matches theoretical models for polycrystalline materials. Notably, the SANS data uncovered a specific size distribution of the Ag_3Sn phase, which was characterized by a sharp interface contrast against the β-Sn matrix, pivotal for understanding the solder's mechanical properties. Interpretation of the SANS and EBSD data sets suggests that the Sn-Ag alloy's performance is significantly influenced by the dispersion and morphology of the Ag_3Sn phase. The presence of nanoscale Ag_3Sn structures, exhibiting a needle-like surface, implies a material optimized for mechanical reinforcement, which is essential for robust electronic connections. The integrated approach offers a novel perspective on the nano structural arrangement of lead-free solders, contributing to the advancement of safer, more reliable electronic materials. The findings have significant implications for the development of next-generation electronic components, reinforcing the transition to environmentally benign manufacturing processes.

1. Introduction

Soldering stands out as a well-established method for metallurgical joining, employing a filler metal, commonly referred to as solder, characterized by a melting point below 425 °C [1]. In the expansive domain of electronic materials, solder assumes a critical function in facilitating the assembly and interconnection. The drive to develop lead-free solders stems from the aim to eliminate Lead (Pb) from both electronic manufacturing processes and waste disposal [2,3]. In manufacturing settings, Pb's higher vapor pressure poses a direct inhalation risk to workers, whereas Sn, being less toxic and having a lower vapor pressure, offers a safer alternative [2]. In response to these concerns, the European Union (EU) enacted the Waste from Electrical and Electronic Equipment (WEEE) and the Restriction of the Use of Certain Hazardous Substances in Electrical and Electronic Equipment (RoHS) directives in 2002 [4,5]. This legislative move prompted extensive efforts to create alternative solder alloys, primarily based on Sn [3]. The resulting lead-free solder alloys have gained popularity, replacing lead-based counterparts in electronic component soldering and packaging [5]. The elimination of lead-based solder was enforced by end-of-life disposal legislation and the EU's RoHS directive [4], making Sn-Ag-Cu eutectic, Sn-Ag, and Sn-Cu eutectic acceptable alternatives. Although Sn-3.5Ag has been widely used during the transition to Pb-free solders, researchers persist in seeking more reliable and cost-effective alternatives. Despite the acceptance of Sn-Ag-Cu (SAC) compositions, particularly on copper substrates, ongoing research explores new Ag-containing solders. These include first-generation Pb-free solders like SAC387 and SAC305, second-generation alloys such as SAC0307 and SAC105, and emerging third-generation alloys that often incorporate Bi and/or Sb into near-eutectic Sn-Ag-Cu compositions [6,7]. Apart from these well-

* Corresponding author.
E-mail address: ae0281@coventry.ac.uk (J. Shanthi Bhavan).

https://doi.org/10.1016/j.matchar.2024.114385
Received 18 June 2024; Received in revised form 31 August 2024; Accepted 14 September 2024
Available online 16 September 2024

known lead free solder alloys, numerous alloys and additives have been suggested and are outlined in many of the review articles [8,9].

Silver plays a crucial role as a primary component in numerous electronic solder alloys. The adoption of Sn-3.5Ag became prevalent in applications where Sn-37 Pb was deemed unsuitable, particularly in scenarios involving the soldering of thick-film silver conductors [10]. With the transition to Pb-free soldering, Sn-3.5Ag has remained in use, and there is a widespread proliferation of new silver-containing solder formulations. Given that these solder alloys are either eutectic or hypoeutectic in composition, the formation of primary Ag_3Sn takes place when the liquid undergoes super cooling concerning the β-Sn liquidus, attributed to challenges in nucleating the β-Sn phase [10,11]. There are only very few studies happened with small angle neutron scattering on lead free solder alloys. In one of the studies, the quantitative parameter characterizing the surfaces of Sn and Ag_3Sn phase microstructures is determined by the before–after ratios of the dominant constant phase elements (CPE) in the equivalent network circuits. This parameter exhibits a linear correlation with the amount of interface between the Sn and Ag_3Sn phases, as measured through small angle neutron scattering [12]. This study presents a novel approach by utilizing an integrated analysis of Small-Angle Neutron Scattering (SANS) and Electron Backscatter Diffraction (EBSD) to provide a detailed nanoscale characterization of the Ag_3Sn phase within Sn-Ag lead-free solder alloys. Unlike previous studies that primarily focus on the morphological aspects of Ag_3Sn, this research delivers a comprehensive quantitative analysis of the size distribution, surface morphology, and specific surface area of Ag_3Sn precipitates. This advanced characterization not only enhances the understanding of the microstructural attributes of these alloys but also provides critical insights into their mechanical reinforcement capabilities, paving the way for the development of more reliable and robust electronic materials. Considerable research has delved into the eutectic formation of Ag_3Sn, identifying its manifestation in three distinct morphological types: plate-like, needle-like, and spheroidal structures. A particular stream of research utilizing controlled unidirectional solidification techniques has demonstrated a morphological evolution in eutectic growth from plate-like to rod-like structures correlated with an increase in solidification speed [10,11,13,14]. Different investigations have suggested that the impact of substantial Ag_3Sn plates is dependent on their positioning within the joint. These studies show that when these plates are oriented in alignment with the direction of crack propagation, they can be of bad effect. Conversely, when the plates are situated in a way that they obstruct or halt the progression of a crack, they can contribute to an extended thermal fatigue life of the joint [15].

The objective of this work is to deepen the understanding of the microstructural properties of Sn-Ag lead-free solder alloys, with a particular emphasis on the Ag_3Sn intermetallic phase. By employing Small-Angle Neutron Scattering (SANS) and Electron Backscatter Diffraction (EBSD), we aim to investigate the phase behavior, grain structure, and the morphological characteristics of Ag_3Sn within these alloys. The study's goal is to explore how different Ag_3Sn morphologies and their distribution and orientation within the solder matrix. This study intends to provide new insights into the microstructural factors that influence the performance of lead-free solders, contributing to the development of more effective and environmentally sustainable electronic materials.

2. Materials and methods

2.1. Small-angle neutron scattering (SANS) experiment

The samples of Sn-Ag (96.5–3.5 % by wt.) alloy under investigation was prepared with dimension 10 × 10 × 1 mm as received. Small-Angle Neutron Scattering (SANS) experiments were conducted at ISIS spallation neutron source using the LARMOR instrument. Neutrons with a wavelength of 1.8 to 13.5 Å were employed to probe the sample structure. The sample was mounted in a sample holder and placed at the center of the neutron beam as shown in the Fig. 1 at room temperature. The incident neutron beam was collimated and directed towards the sample with aperture of 8 × 6 mm. The scattered neutrons were detected on a 2D position sensitive Helium 3 detector of LARMOR instrument, placed at a distance of 4 m from the sample. (See Fig. 2.)

From the 2D scattering cross section, 1D azimuthal averaged data were obtained by considering the magnitude of the scattering vector:

$$q = \sqrt{\left(q\_x\hat{}2 + q\_y\hat{}2\right)}$$

SANS data were collected over a range of scattering vectors Q from 0.004 $Å^{-1}$ to 0.2 $Å^{-1}$. The scattering vector magnitude (Q) was determined using the relation:

$$Q = \frac{4\pi}{\lambda} sin(\theta) \tag{1}$$

where λ is the neutron wavelength and θ is the scattering angle. The scattering angle θ is defined as half the angle between the incident and scattered neutron beams [16,17].

The obtained SANS data were reduced using Mantid software package [18] and was further analyzed using SasView 5.0.6 software package for interpretation. The intensity (I) of the scattered neutrons as a function of Q was plotted. For further analysis, the data were also represented in terms of Q^2 (squared magnitude of the scattering vector), to perform a Guinier analysis.

In the low Q or Guinier region, a linear fit of the natural logarithm of the intensity (ln(I)) versus (Q^2) was performed according to the Guinier approximation [19]:

$$ln(I) = ln(I_0) - \frac{1}{3}Q^2R_g^2 \tag{2}$$

where I_0 is the intensity at Q = 0 and R_g is the radius of gyration [19]. The Guinier model is applicable to any dilute particulate system, irrespective of its shape or size, but restricted to very low values of q (as it involves a Taylor expansion around q = 0).

At the high end of the Q range, a generalised Porod law for the intensity was considered [20]:

$$I(Q) \propto Q^{-(D+1)} \tag{3}$$

where D is the fractal dimension. It relies on the concept that at high enough q, shape information becomes negligible, and the scattering primarily involves mainly reflections from interfaces. A power-law fit in this region provided information about surface roughness and irregularities in the sample [21,22]. For 3D sharp interface, the power law exponent would be fixed to a value of −4.

$$I(q) = \frac{C}{q^4} + Background \tag{4}$$

In the instance of a two-phase system, the Porod Constant, denoted as C can be expressed as [20]:

$$C = 2\pi(\Delta\rho)^2 S_v \tag{5}$$

Here, S_v represents the specific surface area (i.e., the surface area divided by the volume) of the material being investigated, and $\Delta\rho$ denotes the contrast factor between the two phases. By extracting the Porod Constant from experimental data and having knowledge of the contrast factor between the two phases, it becomes possible to determine the specific surface area of the material. This information proves valuable, especially in gaining insights into material porosity, particularly when utilized alongside complementary techniques. [21,22]

To extract detailed information about the sample structure, theoretical models were fitted to the experimental data using the SasView software. Control measurements were conducted to account for background scattering, and any instrumental effects. Blank measurements

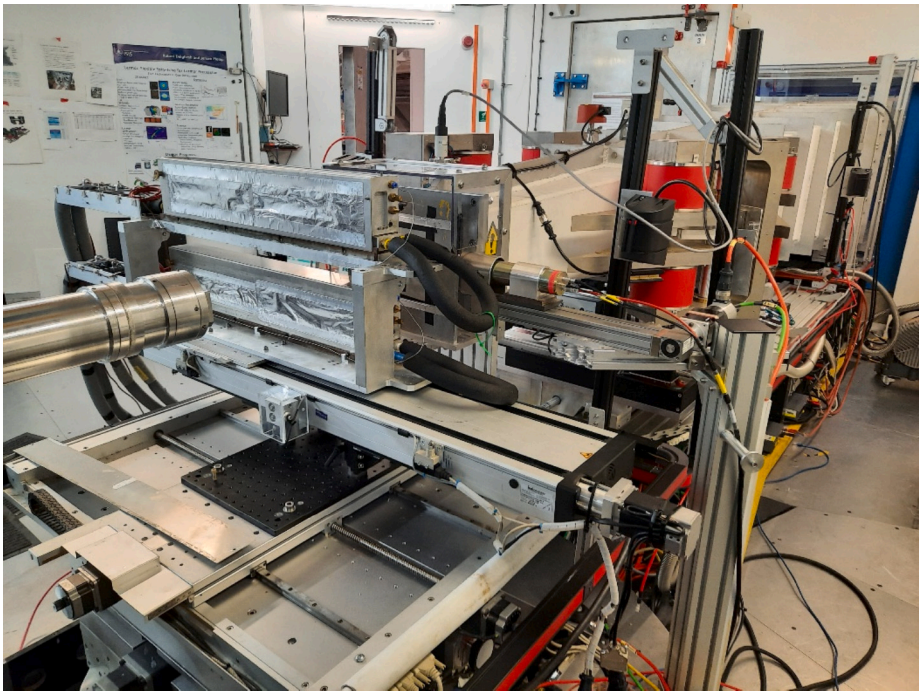

Fig. 1. Experiment setup used for the SANS experiment at LARMOR instrument. The sample is placed in the neutron beam of aperture 6*6 mm, coming from Target station 2 at ISIS facility. The transmitted beam is stopped by a beam stop. The scattered beam is detected by using the He_3 detector placed behind the sample. SANS measurement was done for 15 μA and TRANS measurement was done for 5 μA.

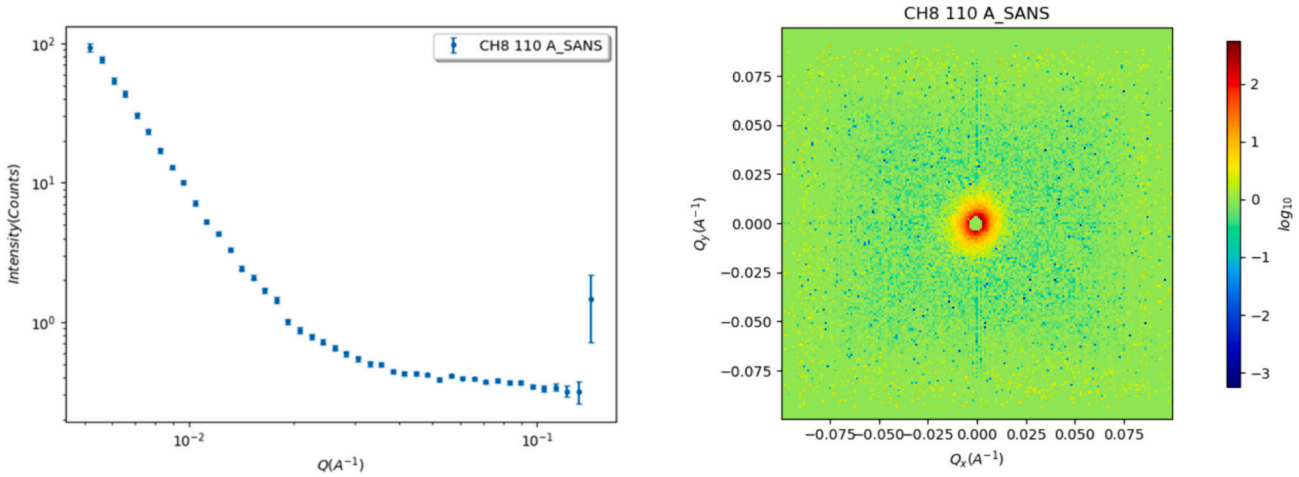

Fig. 2. 1D and 2D plots Intensity vs Q obtained from SANS experiment.

were performed using identical experimental conditions without the sample to measure the background scattering.

2.2. SEM, EDS and EBSD

Scanning Electron Microscopy (SEM) was utilized to acquire high-resolution images of the solder alloy surface topography. The instrument operated at an accelerating voltage of 20 kV, providing a magnified view to identify microstructural components, such as grain boundaries and phase distributions. This facilitated the preliminary morphological assessment of the alloy, allowing for the distinction between different phases based on secondary electron contrast. Energy Dispersive X-ray Spectroscopy (EDS) analysis, integrated with SEM, provided compositional information for the phases identified. Operating under the same electron beam conditions as SEM, EDS detected characteristic X-rays emitted from the sample, enabling the elemental analysis of specific features such as precipitates. The quantitative analysis offered a localized chemical characterization, confirming the presence and distribution of Ag_3Sn phases within the matrix. EBSD analysis was performed on a Symmetry S2® EBSD detector (Oxford Instruments, Abingdon, UK). The EBSD analysis was performed with a fine step size of 3.0781 μm, across a comprehensive raster size of 380 × 286 microns. The SEM was equipped with an EBSD detector, which captured diffraction patterns resulting from the interaction of the electron beam with the crystalline phases. Automated indexing of these patterns provided data on grain orientation, size, and shape. The EBSD analysis yielded an orientation distribution map, highlighting the isotropic nature of the grain structure. Disorientation angle measurements were taken to examine grain boundary character and to assess the degree of crystallinity within the Ag_3Sn phase. The combined SEM, EDS, and EBSD

analyses were pivotal in the multi-scale characterization of the Sn-Ag solder alloys, facilitating a comprehensive understanding of the microstructural dynamics that govern the material's properties.

3. Results and discussion

3.1. Small angle neutron scattering

The specimen comprised interleaved Sn and Ag_3Sn phases, as evident from SEM micrographs shown in the Fig. 5. In this dual-phase system featuring seamless interfaces, the scattering intensity follows the Porod law at higher Q, (see eq. 4, eq. number needs checking).

The value represented by the coefficient A in the equation is connected to how many interfaces there are and the square of the scattering length density difference between the two phases. In Small Angle Neutron Scattering (SANS), this scattering contrast it depends on the atomic composition and density of the phases next to each other. So, the coefficient C is connected to the specific surface in the samples and can be a way to measure the connection between the two phases.

The Q values start from 0.004 and go up to 0.5 A^{-1}, indicating a range of length scales probed in the experiment 150 nm to 1 nm.

The data follows a trend where the intensity decreases as Q increases, which is typical for scattering from metallic systems. The low-Q region (indicative of larger structures) does not exhibit a Guinier plateau, suggesting that the structures are either outside of the Q-range measured or too polydisperse to form a plateau. The high intensity at the lowest Q values could indicate a mass fractal dimension, suggesting a self-similar structure at different length scales.

From Fig. 3, the data at higher Q values does not flatten out, implying a lack of sharp interfaces which would create a Porod tail where $I(Q) \propto Q^{-4}$. Instead, the scattering intensity seems to follow a power law of the form $I(Q) \propto Q^{-\alpha}$, where $\alpha \neq 4$, which is indicative of surface fractals or rough interfaces [20]. A rigorous analytical approach was employed using Eq. 4. The Y-axis label "Intensity Q^4 (Counts $A^{\circ\text{-}\ -16}$)" accurately reflects the data plotted in the figure. The intensity values have been multiplied by Q^4, as indicated by the label, to emphasize the scaling behavior or structural information at different Q values. This transformation is common in small-angle scattering analysis when trying to highlight specific scattering features or regimes. The units of the Y-axis combine the original intensity units (Counts per $A^{\circ\ -1}$ with the Q^4 factor, resulting in the final unit of Counts $A^{\circ\wedge\ -16}$.The fitting process involved fixing the power law exponent at -4, aligning with theoretical predictions for isotropic materials characterized by distinct interfaces. The substantial concordance between the model and the experimental data confirmed the appropriateness of the exponent, accurately representing interface scattering and the stabilization of intensity at elevated QQ values. Quantification of the background term, previously considered an experimental anomaly, revealed its essential role in the accurate interpretation of the data. The smooth decay of intensity without distinct minima or maxima suggests a broad size distribution of scatterers within the sample [20]. The first data point at the lowest Q (0.0052 $Å^{-1}$) has the highest intensity (93.63 counts), Upon review, it was noted that the anomalously high intensity at the lowest QQ value (0.0052 Å-1) could be an artifact, potentially attributable to an issue on the detector's edge. Recognizing the potential to misinterpret this as indicative of larger structures or agglomerates, we have excluded this data point from our analysis. Revised data analysis confirms that this adjustment does not significantly impact our overall conclusions about the microstructural features of the Sn-Ag solder alloys. As Q increases, the intensity decreases rapidly, characteristic of the scattering from smaller structures within the sample. The smooth curve without distinct inflection points implies a complex internal structure with a lack of clear phase separation at the nanoscale. The material's scattering profile suggests it could be composed of clusters or aggregates with a wide range of sizes and possibly a hierarchical structure. (See Fig. 4.)

From the figure, it can be particularly informative for identifying the presence of large particles or aggregates and for evaluating the compactness of structures within the material. In the context of a Sn-Ag sample and considering the Ag_3Sn and beta-Sn phases, The plateau or relatively flat region at the lower Q^4 values indicates that the sample contains large scattering entities. For the Sn-Ag alloy, this could signify the presence of large Ag_3Sn particles or clusters. The intensity in this region is generally low, which could suggest that these entities are relatively sparse or that the contrast between the Ag_3Sn particles and the surrounding matrix is not very high. The sharp increase in intensity at the highest Q^4 values, especially the point with a very large error bar, could be due to several factors: It might indicate the presence of small particles or features within the sample, which could be fine precipitates of Ag_3Sn or beta-Sn. The large error bar on the rightmost data point suggests there may be uncertainty or variability in this region of the scattering data, possibly due to instrument noise, data processing, or a low number of counts. The presence of Ag_3Sn can often be identified by characteristic peaks or changes in the slope of the plot, corresponding to the distances between particles or features within the phase. However, without distinct peaks, it may suggest that Ag_3Sn is either well dispersed or not forming large enough features to create a distinct scattering pattern. For the beta-Sn phase, which is the matrix in which Ag_3Sn precipitates are embedded, one would expect a more uniform scattering intensity if it forms a continuous phase without significant internal structure at the length scales probed by the SANS experiment.

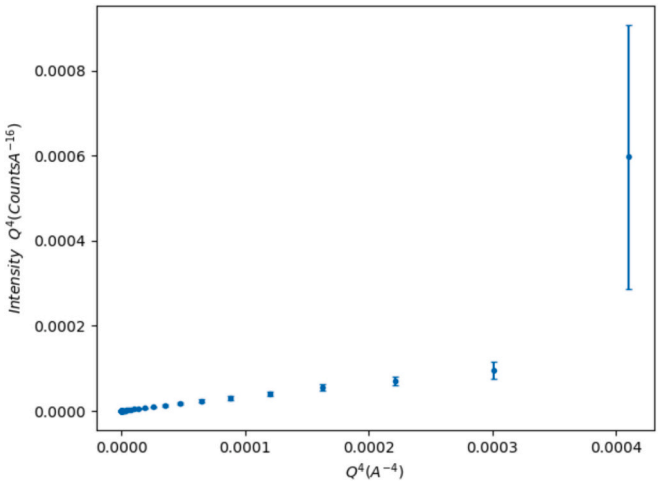

Fig. 3. Plot of Porod region obtained.

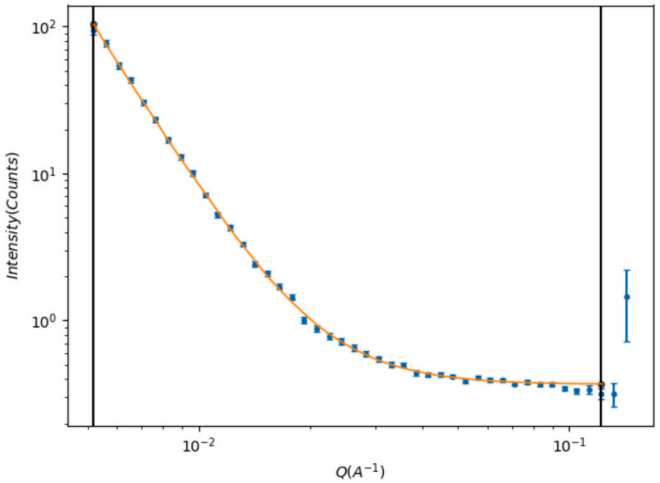

Fig. 4. Porod region fitted using power law for the Ag_3Sn phase (needle shape).

3.2. Porod fitted using power law to delve into Ag3Sn details

The combination of Ag_3Sn data, power-law fitting, and SLD calculations provide a comprehensive picture of the Ag_3Sn phase in the material, revealing details about the size, distribution, and nature of the scattering entities at the nanoscale. This analysis is crucial for tailoring the material's properties for specific applications where the nanostructure plays a critical role in the material's performance. The curve fitting is done using a power law, which is often used to describe scattering from fractal or self-similar structures. The dashed line represents the fit to the data. The fitting parameters include a power (A_power), scale (B_scale), scattering length density contrast (B_sld), and a radius (B_radius). A_power of 3.8813 suggests a fractal dimension, which is related to the slope of the plot in the log-log scale. This value is typical for surface fractal structures. B_scale, the scaling factor, correlates with the intensity of scattering at low Q and could be related to the volume fraction of the scattering entities. B_sld is the scattering length density contrast between the particles and the surrounding matrix. A value of 3.46×10^{-6} Å^{-2} indicates a moderate contrast, which is crucial for the visibility of the Ag_3Sn phase in the SANS data. B_radius is the characteristic length scale of the scattering entities, here fitted as 27.866 Å with a substantial error, suggesting there is a distribution of sizes.

The Scattering Length Density (SLD) values are essential for interpreting neutron scattering data as they represent the coherent neutron scattering length per unit volume. The scattering length equation, is typically expressed in terms of the scattering length b:

$$\frac{d\sigma}{d\varphi} = |b|^2$$

For Ag_3Sn with a mass density of 10.49 g/cm^3 and a neutron wavelength of 6.0 Å, the neutron SLD is calculated as 3.43e-6 - i 7.57e-9 Å^{-2}. This complex number indicates that there is both a real part, which contributes to the scattering intensity, and an imaginary part, which is related to absorption. The neutron inc. xs and abs. xs are the incoherent and absorption cross-sections, respectively, providing additional details on how neutrons interact with the material. The inc. xs is quite low (0.0254 1/cm), suggesting that incoherent scattering is not significant in this case. The 1/e length is a measure of how far neutrons can penetrate into the material before their intensity drops to 1/e of its original value. For Ag_3Sn, its 0.107 cm, meaning neutrons can probe deep into the sample, which is advantageous for SANS.

Significant investigative efforts have been dedicated to understanding the eutectic crystallization of Ag_3Sn, which is observed to occur in three specific morphological varieties: planar, acicular, and globular forms. Certain studies, employing methodical directional solidification processes, have revealed a progression in the eutectic structures from flat to cylindrical shapes, a transformation that is associated with the acceleration of the solidification rate [10,11,13,14].

The SANS data and model fitting suggest that the Ag_3Sn phase forms structures with a specific needle-like surface or mass dimension, as indicated by the power law behavior. The characteristic size of these structures is on the order of tens of angstroms, which aligns with the presence of nanoscale features such as precipitates or clusters within the material. The SLD values are consistent with the presence of Ag_3Sn phase and provide the necessary contrast for the SANS measurement. The moderate contrast between the Ag_3Sn phase and the matrix indicates that the boundaries of the Ag_3Sn particles are well-defined at the nanoscale, which is critical for interpreting the size and distribution of these particles. The radius obtained from the fitting gives an average size for the structures contributing to the SANS signal, which can be related to the physical features in the material, such as precipitates or other phase inclusions of Ag_3Sn. The analysis suggests that the material has a complex internal structure with a distribution of particle sizes and a fractal dimension indicative of a specific type of disorder or surface roughness. This information can be critical for understanding the material's mechanical properties, as nanoscale precipitates can strengthen materials by hindering dislocation movement.

The SEM image clearly shows elongated, needle-like structures which is the Ag_3Sn phase. This was confirmed with the EDS analysis. This confirmation supports the selection of an elliptical cylinder model for the SANS data analysis, as the needles would scatter neutrons in a manner similar to elliptical cylinders. The elliptical cylinder model used in the SANS data analysis is appropriate for representing the needle-like morphology observed in the micrograph. The fitting parameters derived from the model, such as the radius and length of the cylinders, can be directly related to the dimensions of the needle-like Ag_3Sn structures. The length scale provided by the SANS model, B_radius ~27.866 Å, can be compared with the actual sizes of the needles in the micrograph. The needle-like morphology of the Ag_3Sn phase would have significant implications for the mechanical properties of the material. Such structures can act as reinforcement, affecting the tensile strength and potentially improving the material's resistance to deformation. Additionally, the orientation of these needle-like structures can impart anisotropy to the material's properties, which could be crucial for applications requiring directional strength or conductivity.

3.3. 2D SANS analysis

Fig. 6 shows the intensity of neutron scattering as a function of the scattering vector Q from a selected sector of a 2D Small-Angle Neutron Scattering (SANS) analysis. This type of data is typically used to understand the scattering characteristics of a sample in a specific direction or angular range. The plot follows a trend where the scattering intensity decreases with increasing Q. This is a common feature in SANS data and indicates the presence of structures in the sample at different length scales. The intensity at the lowest Q values (towards the left of the plot) corresponds to the largest structures within the sample. Since the intensity keeps decreasing, it suggests that the large structures are not the only contributors to the scattering. The smooth decrease in intensity across this range without distinct peaks or troughs suggests a lack of periodic structures or sharp interfaces within the sample. It is likely that the sample has a random or amorphous structure on the length scales probed by these Q values. Because the data represents a selected sector from a 2D SANS pattern, it suggests that the analysis is interested in angular-dependent scattering.

3.4. Zimm plot vs EBSD

A Zimm plot shown in in Fig. 7 is used to extract the particle size distribution from the data. A Zimm plot from SANS data gives information on the nanoscale structure, including the size distribution of scattering centers (which could be grains, precipitates, or voids) and the overall shape of the scatterers. For that Zim plot is created between inverse intensity and Q2. The plot shows a trend where the inverse intensity increases with Q^2 until a certain point where there is a sharp drop-off. This pattern indicates that there are structural features in the Sn-Ag alloy with a characteristic size; the scattering is intense at small angles (low Q^2 values) and then decreases significantly. The drop-off point can be associated with the size of the scattering entities. A larger Q^2 value at the drop-off would suggest smaller entities and vice versa. The EBSD data comprises grain size distribution, a microstructure map, and disorientation angle distribution. The histogram shows the number of grains corresponding to specific pixel counts. This data indicates a wide grain size distribution with most grains being small (low pixel count), but with some larger grains present (up to 2121 pixels). The map represents different grains in the alloy. The variety of colours and the boundaries between them suggest that the alloy has a polycrystalline structure with grains of varying orientations. The disorientation plot compares the theoretical disorientation angle distribution for a random polycrystalline material with the actual distribution from the EBSD data (shown in Fig. 8). The comparation analysis suggests that the distribution of disorientation angles closely matches theoretical predictions for

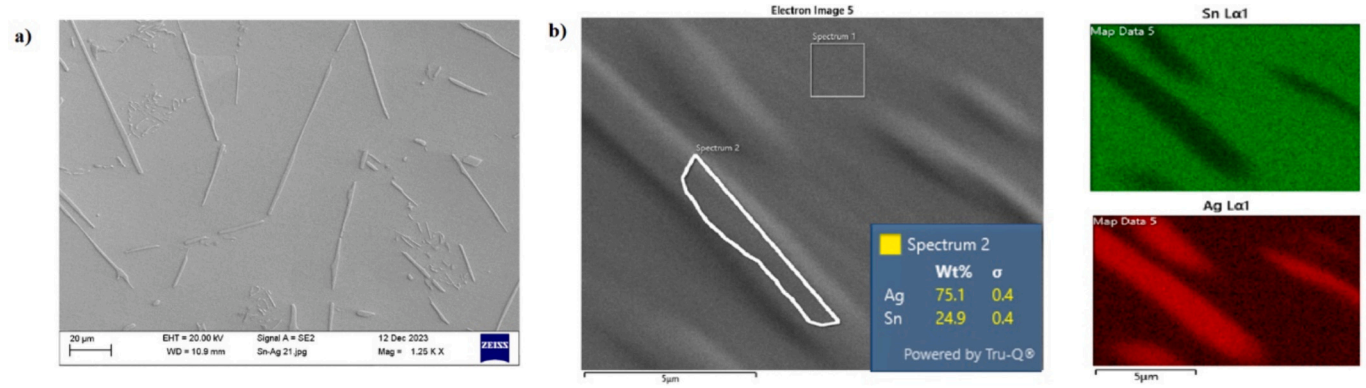

Fig. 5. a)SEM image of Sn-Ag showing Ag_3Sn phase (needle shape) b) Colour mapping focusing on Ag_3Sn.

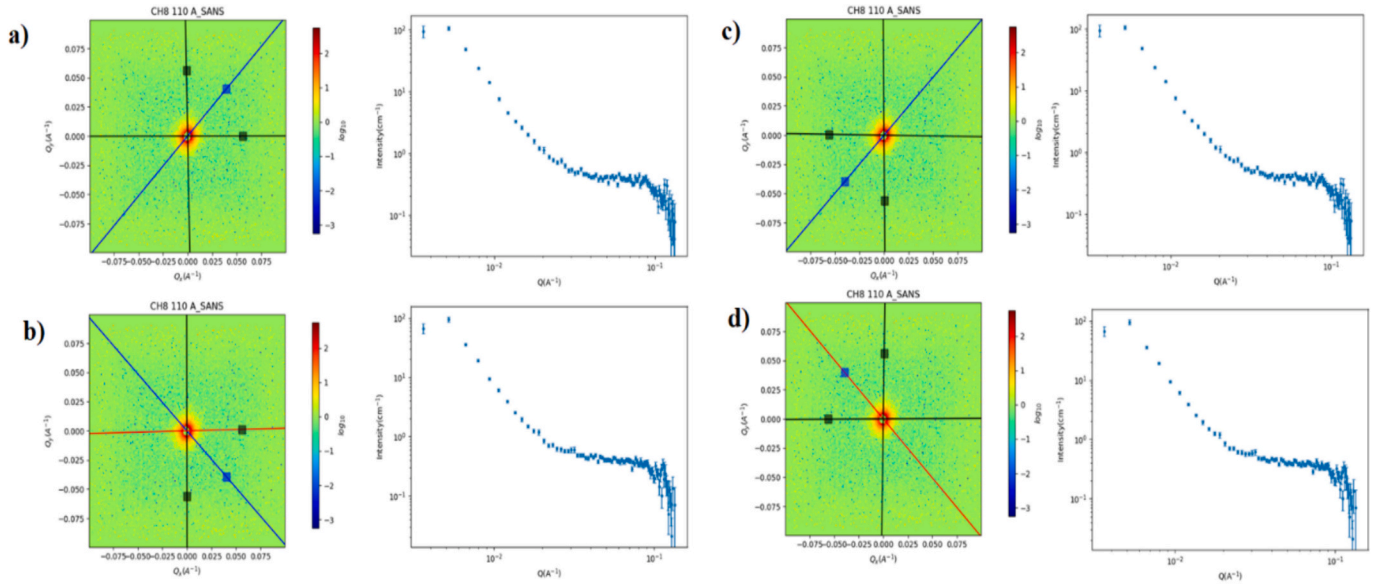

Fig. 6. Intensity of neutron scattering of a sector of a 2D SANS.

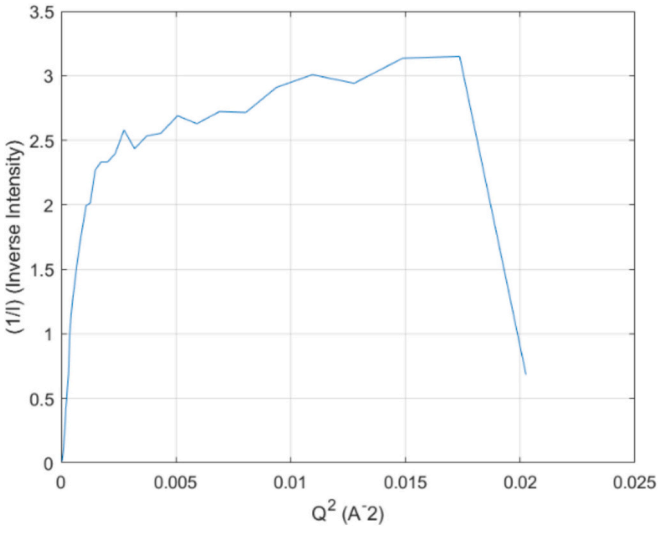

Fig. 7. A Zimm plot used to extract the particle size distribution from the data.

random grain boundaries, with some deviation that could be due to the presence of texture or preferred grain orientations. The grain size and disorientation data suggest that the Sn-Ag alloy has multiple phases. The larger grains could be indicative of the β-Sn phase, which is ductile and can grow to larger sizes, while the presence of smaller grains might be associated with the formation of intermetallic Ag_3Sn phases. The sharp decline in the Zimm plot could correspond to the scattering from the Ag_3Sn phases. If this drop correlates with the size of the smaller grains observed in the EBSD data, it suggests that the Ag_3Sn phases are finely dispersed throughout the β-Sn matrix. The microstructure map and the disorientation angle distribution imply that the material has a mixed texture with no strong preferential orientation.

4. Conclusion

The comprehensive analysis has quantitatively characterized the microstructural attributes of Sn-Ag lead-free solder alloys, emphasizing the critical role of the Ag_3Sn intermetallic phase. Through Small-Angle Neutron Scattering (SANS), the study discerned a pronounced scattering intensity attributed to Ag_3Sn precipitates, with a peak at $Q \approx 0.05–0.1$ $Å^{-1}$, indicative of coherent scattering entities within the β-Sn matrix. Electron Backscatter Diffraction (EBSD) corroborated these findings, revealing a broad grain size distribution with a mean area-weighted diameter of approximately 289.1 pixels, corresponding to

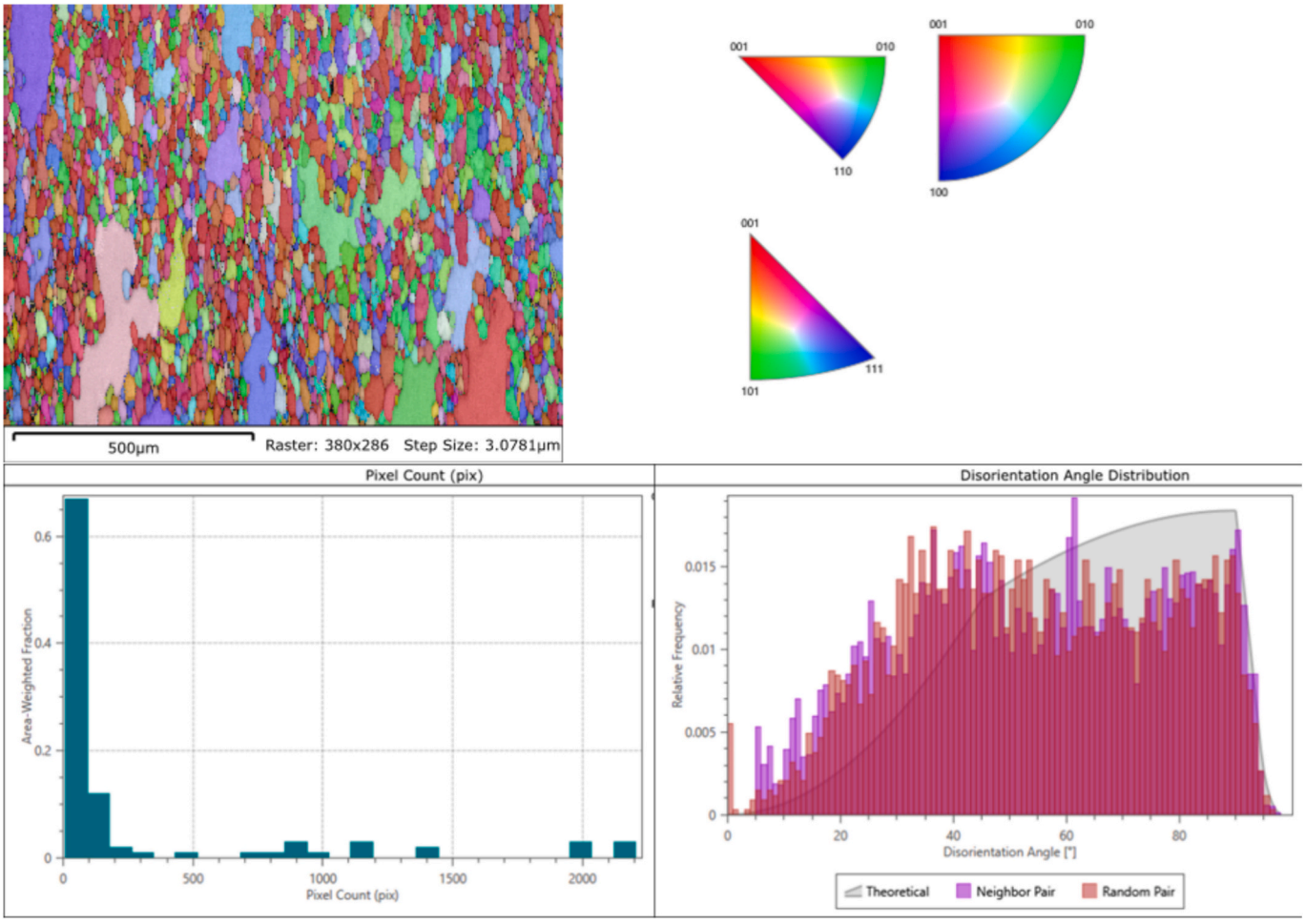

Fig. 8. EBSD results of the sample.

the Ag_3Sn phase dispersed uniformly throughout the solder matrix. The specific surface area calculated from the SANS data, utilizing the Porod law, suggests a highly refined microstructure, with Ag_3Sn precipitates exhibiting a fractal dimension indicative of complex surface morphology. These precipitates, ranging in size but generally maintaining a submicron presence, contribute to the solder's mechanical fortitude, providing a nanoscale reinforcement that is likely to underpin the solder's performance in electronic applications. Moreover, the detailed EBSD analysis showcased a random orientation distribution, with a disorientation angle analysis congruent with theoretical models for polycrystalline aggregates, affirming a lack of preferential grain orientation. This isotropic grain structure is conducive to uniform stress distribution across the solder joints, enhancing their mechanical reliability. The investigation into the Sn-Ag alloy system elucidates the nanostructured Ag_3Sn phase as a determinant factor in defining the solder's material properties. The quantitative assessment of phase dimensions and distribution has significant implications for the predictive modeling of solder behavior under operational conditions. This study advances the material science of lead-free solders by providing a thorough understanding of the intrinsic properties that dictate performance, offering critical insights for the engineering of next-generation electronic materials with superior mechanical robustness and reliability.

CRediT authorship contribution statement

Jayesh Shanthi Bhavan: Writing – original draft, Validation, Project administration, Methodology, Investigation, Formal analysis, Data curation, Conceptualization. **Gokulnath Kadavath:** Writing – review & editing, Software, Methodology. **Dirk Honecker:** Writing – review & editing, Validation, Methodology, Investigation, Formal analysis. **Ashwath Pazhani:** Writing – review & editing, Validation, Resources.

Declaration of generative AI and AI-assisted technologies in the writing process

During the preparation of this work the authors used Generative AI to rephrase the literature and improving language. After using this tool/service, the authors reviewed and edited the content as needed and take full responsibility for the content of the publication.

Declaration of competing interest

The authors declare that they have no known competing financial interests or personal relationships that could have appeared to influence the work reported in this paper.

Data availability

The raw/processed data required to reproduce these findings cannot be shared at this time as the data also forms part of an ongoing study.

Acknowledgements

The authors acknowledge the support from British Council's Going Global Partnerships Grant (IND/CONT/G/23-24/26). The authors would also like to thank ISIS Neutron and Muon Source, Science and

Technology Facilities Council, Rutherford Appleton Laboratory, UK for providing the necessary beam time and the subsequent help to extract and interpret results.

References

[1] F. van der Hoek, Soldering and brazing, in: A. Davidson (Ed.), Handbook of Precision Engineering: Volume 5 Joining Techniques, Macmillan Education UK, London, 1972, pp. 110–229, https://doi.org/10.1007/978-1-349-01020-2_4.

[2] T.R. Bieler, T. Lee, Lead-free Solder, in: Encyclopedia of Materials: Science and Technology, Jan. 2010, pp. 1–12, https://doi.org/10.1016/B978-008043152-9.02239-9.

[3] M. Sarkar, F. Gulshan, A.R.M.H. Rashid, M. Hasanuzzaman, A review of TiO2-nanoparticle reinforced Lead-free solder composites used in electronic components soldering, Encyclop. Mater. Electron. 1–3 (Jan. 2023) 456–463, https://doi.org/10.1016/B978-0-12-819728-8.00002-4.

[4] M. Hedemann-Robinson, The EU directives on waste electrical and electronic equipment and on the restriction of use of certain hazardous substances in electrical and electronic equipment: adoption achieved, Europ. Energy Environ. Law Rev. (2003) 52–60 [Online]. Available: http://www.kluwerlawonline.com/api/Product/CitationPDFURL?file=JournalsEELREELR2003007.pdf.

[5] M. Shahabuddin, et al., A review of the recent development, challenges, and opportunities of electronic waste (e-waste), Int. J. Environ. Sci. Technol. 20 (4) (2023) 4513–4520, https://doi.org/10.1007/s13762-022-04274-w.

[6] D.A. Shnawah, M.F.M. Sabri, I.A. Badruddin, A review on thermal cycling and drop impact reliability of SAC solder joint in portable electronic products, Microelectron. Reliab. 52 (1) (Jan. 2012) 90–99, https://doi.org/10.1016/J.MICROREL.2011.07.093.

[7] P. Darbandi, T.R. Bieler, F. Pourboghrat, T. Lee, The effect of cooling rate on grain orientation and Misorientation microstructure of SAC105 solder joints before and after impact drop tests, J. Electron. Mater. 43 (7) (2014) 2521–2529, https://doi.org/10.1007/s11664-014-3176-4.

[8] M. Abtew, G. Selvaduray, Lead-free solders in microelectronics, Mater. Sci. Eng. R. Rep. 27 (5–6) (Jun. 2000) 95–141, https://doi.org/10.1016/S0927-796X(00)00010-3.

[9] M. Bharath Krupa Teja, A. Sharma, S. Das, K. Das, A review on nanodispersed lead-free solders in electronics: synthesis, microstructure and intermetallic growth characteristics, J. Mater. Sci. 57 (19) (2022) 8597–8633, https://doi.org/10.1007/s10853-022-07187-8.

[10] Y. Cui, J.W. Xian, A. Zois, K. Marquardt, H. Yasuda, C.M. Gourlay, Nucleation and growth of Ag3Sn in Sn-Ag and Sn-Ag-Cu solder alloys, Acta Mater. 249 (May 2023) 118831, https://doi.org/10.1016/J.ACTAMAT.2023.118831.

[11] H.Y. Lu, H. Balkan, K.Y.S. Ng, Effect of Ag content on the microstructure development of Sn-Ag-Cu interconnects, J. Mater. Sci. Mater. Electron. 17 (3) (2006) 171–178, https://doi.org/10.1007/s10854-006-6758-y.

[12] T. Hurtony, et al., Characterization of the microstructure of tin-silver lead free solder, J. Alloys Compd. 672 (Jul. 2016) 13–19, https://doi.org/10.1016/J.JALLCOM.2016.02.177.

[13] H. Esaka, K. Shinozuka, M. Tamura, Evolution of structure Unidirectionally solidified Sn–Ag₃Sn eutectic alloy, Mater. Trans. 46 (5) (2005) 916–921, https://doi.org/10.2320/matertrans.46.916.

[14] M. Şahin, E. Çadirli, The effects of temperature gradient and growth rate on the microstructure of directionally solidified Sn–3.5Ag eutectic solder, J. Mater. Sci. Mater. Electron. 23 (2) (2012) 484–492, https://doi.org/10.1007/s10854-011-0422-x.

[15] S.K. Kang, et al., The microstructure, thermal fatigue, and failure analysis of near-ternary eutectic Sn-Ag-Cu solder joints, Mater. Trans. 45 (3) (2004) 695–702, https://doi.org/10.2320/matertrans.45.695.

[16] O. Kratky, The importance of x-ray small-angle scattering in colloid research, in: K. Hummel, J. Schurz (Eds.), Dispersed Systems, Steinkopff, Darmstadt, 1988, pp. 1–14.

[17] L.A. Feigin, D.I. Svergun, G.W. Taylor, Principles of the theory of X-ray and neutron scattering, in: L.A. Feigin, D.I. Svergun, G.W. Taylor (Eds.), Structure Analysis by Small-Angle X-Ray and Neutron Scattering, Springer US, Boston, MA, 1987, pp. 3–24, https://doi.org/10.1007/978-1-4757-6624-0_1.

[18] Mantid Software [Online]. Available, https://www.mantidproject.org/index.html, 2024.

[19] S.A. Rice, Small angle scattering of X-rays. A. Guinier and G. Fournet. Translated by C. B. Wilson and with a bibliographical appendix by K. L. Yudowitch. Wiley, New York, 1955. 268 pp. $7.50, J. Polym. Sci. 19 (93) (Mar. 1956) 594, https://doi.org/10.1002/pol.1956.120199326.

[20] D.F.R. Mildner, P.L. Hall, Small-angle scattering from porous solids with fractal geometry, J. Phys. D. Appl. Phys. 19 (8) (1986) 1535, https://doi.org/10.1088/0022-3727/19/8/021.

[21] L.A. Feigin, D.I. Svergun, Structure Analysis by Small-Angle X-Ray and Neutron Scattering, Springer US, Boston, MA, 1987, https://doi.org/10.1007/978-1-4757-6624-0.

[22] O. Kratky, The importance of x-ray small-angle scattering in colloid research, in: K. Hummel, J. Schurz (Eds.), Dispersed Systems, Steinkopff, Darmstadt, 1988, pp. 1–14.